Front. Chem. Sci. Eng. 2023, 17(6): 679–690
https://doi.org/10.1007/s11705-022-2266-8

RESEARCH ARTICLE

Direct pyrolysis to convert biomass to versatile 3D carbon nanotubes/mesoporous carbon architecture: conversion mechanism and electrochemical performance

Chenxi Xu[1*], Shunli Li[1*], Zhaohui Hou[2], Liming Yang[3], Wenbin Fu[4], Fujia Wang[4], Yafei Kuang[1], Haihui Zhou (✉)[1], Liang Chen (✉)[2]

1 College of Chemistry and Chemical Engineering, Hunan University, Changsha 410082, China
2 Key Laboratory of Hunan Province for Advanced Carbon-Based Functional Materials, School of Chemistry and Chemical Engineering, Hunan Institute of Science and Technology, Yueyang 414006, China
3 Key Laboratory of Jiangxi Province for Persistent Pollutants Control and Resources Recycle, Nanchang Hangkong University, Nanchang 330063, China
4 School of Materials Science and Engineering, Georgia Institute of Technology, Atlanta, GA 30332, USA

Abstract The massive conversion of resourceful biomass to carbon nanomaterials not only opens a new avenue to effective and economical disposal of biomass, but provides a possibility to produce highly valued functionalized carbon-based electrodes for energy storage and conversion systems. In this work, biomass is applied to a facile and scalable one-step pyrolysis method to prepare three-dimensional (3D) carbon nanotubes/mesoporous carbon architecture, which uses transition metal inorganic salts and melamine as initial precursors. The role of each employed component is investigated, and the electrochemical performance of the attained product is explored. Each component and precise regulation of their dosage is proven to be the key to successful conversion of biomass to the desired carbon nanomaterials. Owing to the unique 3D architecture and integration of individual merits of carbon nanotubes and mesoporous carbon, the as-synthesized carbon nanotubes/mesoporous carbon hybrid exhibits versatile application toward lithium-ion batteries and Zn-air batteries. Apparently, a significant guidance on effective conversion of biomass to functionalized carbon nanomaterials can be shown by this work.

Keywords biomass, direct pyrolysis, 3D CNTs/MC hybrid, lithium-ion batteries, Zn-air batteries

Received August 3, 2022; accepted September 26, 2022

E-mails: haihuizh@163.com (Zhou H.), clvilance@163.com (Chen L.)

* These authors contributed equally to this work.

1 Introduction

Carbon materials contribute greatly to the development of most aspects of our society, including electronic, biomedicine, energy and environment [1–3]. Not only conventional carbon materials existing in the form of graphite, diamond and activated carbon, but the next-generation carbon nanomaterials, such as zero-dimensional fullerenes, one-dimensional carbon nanotubes (CNTs), two-dimensional graphene and three-dimensional (3D) carbon hybrids, are gradually drawing our attentions in recent years [4–6]. These new carbon nanomaterials show charming electrical, thermal and mechanical properties, which display great potential in practical applications of energy and environment [7–9].

The methods of carbon nanomaterials preparation, such as chemical vapor deposition (CVD), arc discharge, glow discharge, laser ablation, have been developed for decades [10]. However, the employed carbon sources for preparing carbon nanomaterials are nonrenewable coal and petroleum products, like methane, ethane, ethylene and ethyne, which inevitably leads to energy shortage and environment pollution [11,12]. Exploring low-cost, environmentally friendly and reproducible carbon source becomes the pivot to extensive application of carbon nanomaterials.

Biomass, as a huge and renewable resource, can be readily attained with a production level of over hundreds of billion tons per year by photosynthesis of carbon dioxide, water and sunlight. It is estimated that nearly 30 billion tons of biomass can be produced every year from

agriculture, industry and forestry [13,14]. Undoubtedly, rational and effective utilization of these biomass emerges as an exigent issue.

The feasibility of transforming biomass to biofuels and chemicals, such as ethanol, phenol, methane, benzene and their derivatives has been confirmed by previous studies [15–17]. Continuously, great efforts have been made to the conversion of biomass to carbon nanomaterials, and a variety of carbon nanomaterials (including nanocapsules, carbon nanoribbons, CNTs, graphene nanosheets arrays, carbon nanospheres, etc.) have been successfully synthesized [18–21]. As surveyed, previously reported works mainly focus on the effect of biomass precursors on the carbonization of biomass [22], the effect of morphology, structure and composition of biomass-derived carbon on their electrochemical performance [13], pore generation mechanism [23], different activation strategies [24] and the application of biomass-derived carbon [25]. In spite of these achieved progress, it is still found that the actual fabrication process always involves expensive setup or needs to be conducted under harsh conditions. Besides, the yield of carbon nanomaterials is usually limited. Most importantly, the involved synthesis procedure is considered to be much complex, thus resulting in unclear conversion mechanism and uncontrollable synthesis of carbon nanomaterials. Hence, developing a facile and scalable approach to directly convert biomass to carbon nanomaterials will greatly benefit our real-world carbon material applications.

Recently, Guo et al. [26] for the first time adopted a soft-template multi-step annealing method to directly synthesize bamboo-like CNTs/Fe_3C nanoparticles hybrid by using PEG-PPG-PEG Pluronic, melamine and iron nitrate as C, N and Fe sources, respectively, and demonstrated its efficient activity towards oxygen reduction reaction (ORR). Though the formation mechanism of CNTs/Fe_3C hybrid is not yet studied by the researchers, this surprising finding tells us the possibility of converting biomass to carbon nanomaterials by direct annealing process. In spired by this work and the growing mode of carbon nanomaterials by conventional CVD, we conclude that three components, carbon sources (CH_4, C_2H_4, etc.), catalysts (Fe, Co, Ni, etc.) and reductive gas (like C_2H_2) need to be simultaneously taken into account for successful synthesis of carbon nanomaterials. Hereby, we envisage if biomass is used as carbon source, and catalysts as well as reductive gas are provided at the same time, can carbon nanomaterials be produced by direct one-step pyrolysis?

To check our supposition, in this work, we employed series of different biomass (including yeast, chitosan, glucose and sucrose) and transition metal inorganic salts (including Fe, Co and Ni salts) as carbon sources and catalyst precursors. Meanwhile, melamine was used to release NH_3, which plays a role of reductive gas. The biomass, catalyst and melamine were blended by a simple grinding strategy, and then underwent direct pyrolysis process at high temperature to attain carbon nanomaterials. Herein, the role of each employed component was systematically investigated, and the possible conversion mechanism was also explored. By series of comparison experiments, we affirm the viability of direct pyrolysis to convert biomass to 3D CNTs/mesoporous carbon (MC) architecture. Moreover, it can be observed that the presence of each component and precise control of their dosage become the prerequisite to successful preparation of desired carbon nanomaterials. Due to the unique 3D architecture and combination of individual advantages of CNTs and MC, our prepared versatile CNTs/MC hybrid displays great potential as an anode material for lithium-ion batteries (LIBs) and a catalyst for ORR in Zn-air batteries (ZABs). Obviously, our results offer valuable guidance on effective conversion of biomass to usable high value-added carbon nanomaterials.

2 Experimental

2.1 Synthesis of CNTs/MC hybrid

Briefly, commercial yeast was firstly mixed with $FeCl_3 \cdot 6H_2O$ and melamine with a mass ratio of 10/3/100, and then ground into uniform fine powder by mortar. The obtained powder was subsequently subjected to high-temperature pyrolysis at 800 °C for 2 h to get the fluffy black product, which is denoted as CNTs/MC-Y (10/3/100) hybrid. To investigate the role of biomass precursor, we substituted yeast with chitosan, glucose and sucrose, respectively, and synthesized the corresponding carbon products, which were marked as CNTs/MC-C (10/3/100), CNTs/MC-G (10/3/100) and CNTs/MC-S (10/3/100), respectively. For better comparison, the control samples named as CNTs/MC-Y (*x*/*y*/*z*) were also produced under similar conditions except for changing the dosages of three different components. Herein, the value of *x*/*y*/*z* stands for the mass ratio of yeast, $FeCl_3 \cdot 6H_2O$ and melamine. In addition to this, pure MC was also prepared by directly annealing yeast at 800 °C for 2 h.

3 Results and discussion

3.1 Preparation and characterization of CNTs/MC-Y hybrids

Figure 1 depicts the schematic diagram of the synthesis of 3D CNTs/MC-Y (10/3/100) hybrid. In brief, yeast was firstly mixed with $FeCl_3 \cdot 6H_2O$ and melamine in a mass ratio of 10/3/100 to get the initial composite precursor, and then directly pyrolyzed to attain the fluffy black

product, CNTs/MC-Y (10/3/100) hybrid.

The morphology and microstructure of CNTs/MC-Y (10/3/100) hybrid are explored by scanning electron microscope (SEM) and transmission electron microscope (TEM), as shown in Fig. 2. From the SEM image in Fig. 2(a), we observed that CNTs interweave with MC, forming typical 3D architecture. The existence of MC not only provides the growing substrate for CNTs, but inhibits the bundling of CNTs. Meanwhile, the formation of CNTs mitigates the agglomeration of MC, which can be reflected from the SEM image of pure MC (see Fig. S1, cf. Electronic Supplementary Material, ESM) and the Brunauer–Emmett–Teller (BET) results (vide infra). Figures 2(b–g) present the TEM images and the corresponding elemental mapping images of CNTs/MC-Y (10/3/100) hybrid. The appearance of bamboo-like nanotubes indicates successful N doping in CNTs [26,27]. Meanwhile, the existence of nanoparticles with a diameter ranging from several nanometers to tens of nanometers can be assigned to the formation of Fe_2O_3, which is confirmed by the high-resolution TEM image (HRTEM, see Fig. S2, cf. ESM) and O and Fe mapping images. From the HRTEM image, the interplanar spacing of 0.207 nm corresponds to the d_{202} spacing of Fe_2O_3, demonstrating the formation of Fe_2O_3. Also, it was evidenced that Fe_2O_3 nanoparticles are surrounded by exterior crystalline carbon layers, indicating its key role of catalytic graphitization of carbon layers [28–30]. The C and N mapping images in Figs. 2(d) and 2(e) imply uniform distribution of N element throughout the whole structure of CNTs/MC-Y (10/3/100) hybrid. Besides, as reflected from the TEM images in Figs. 2(c) and S3 (cf. ESM), the Fe_2O_3 nanoparticles locate on the top side of CNTs, implying the growth of CNTs follows typical "tip-growth" mode [31,32].

To measure the phase structure and defect nature of CNTs/MC-Y (10/3/100) hybrid, X-ray diffraction (XRD) and Raman techniques were exploited, as displayed in Fig. 3. Compared with the XRD pattern of pristine CNTs (supplied by Shenzhen Nanotech Port Co., Ltd.) in Fig. 3(a), both of MC and CNTs/MC-Y (10/3/100) hybrid display a much weakened and broad peak at ~26°, indicating less crystallized carbon structure. Additionally, the residual peaks at ~24°, ~33° and ~41° belong to the XRD peak of Fe_2O_3 (PDF#33-0664), while the other weak peaks at ~43° and ~51° indicate the existence of tiny Fe_3C (PDF#35-0772). As betrayed from the Raman spectra in Fig. 3(b), all samples display two typical peaks located at 1350 and 1580 cm^{-1}, corresponding to the D band and G band of carbon materials. It is widely accepted that the intensity ratio of these two bands reflects the defect density of carbon materials [33–35].

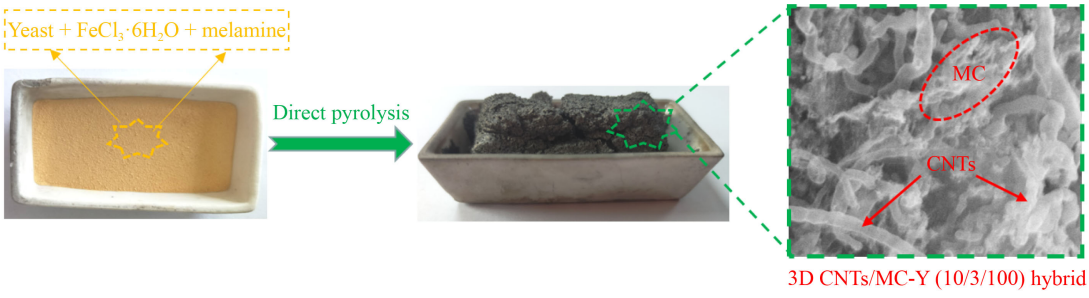

Fig. 1 Schematic diagram of the synthesis of 3D CNTs/MC-Y (10/3/100) hybrid.

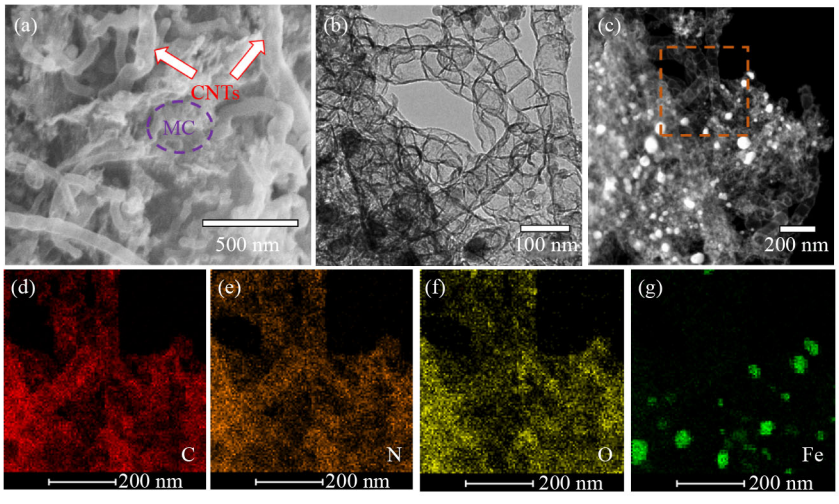

Fig. 2 (a) SEM, (b) TEM, (c) scanning transmission electron microscopy images and the corresponding element mapping images of (d) C, (e) N, (f) O and (g) Fe of CNTs/MC-Y (10/3/100) hybrid.

The intensity ratio of D band to G band (I_D/I_G) of CNTs/MC-Y (10/3/100) hybrid is 1.07, which proves larger than those of MC (0.94) and commercial CNTs (0.85), indicating higher defect density. The higher defect density of MC than CNTs suggests the formation of amorphous carbon structure in MC, which is consistent with the result reported by previous literature [36].

The specific surface area (SSA) and pore distribution state of samples were measured by typical BET method (see Fig. S4, cf. ESM). The N_2 adsorption/desorption isothermal curves in Fig. S4(a) belong to type-IV characteristic, demonstrating mesoporous feature. Based on the BET result (see Table S1, cf. ESM), the SSA for CNTs/MC-Y (10/3/100) hybrid (225.5 $m^2 \cdot g^{-1}$) is much larger than those for MC (58.6 $m^2 \cdot g^{-1}$) and CNTs (83.1 $m^2 \cdot g^{-1}$). In the meantime, it was evidenced that the pore volume for CNTs/MC-Y (10/3/100) hybrid (0.622 $cm^3 \cdot g^{-1}$) is much larger than those for MC (0.0036 $cm^3 \cdot g^{-1}$) and CNTs (0.013 $cm^3 \cdot g^{-1}$). The increased SSA and pore volume for CNTs/MC-Y (10/3/100) hybrid mainly originate from the formation of 3D architecture, which not only prohibits the agglomeration of MC and bundling of CNTs, but also creates abundant pores between MC and CNTs. As seen from Fig. S4(b), two typical peaks at ~2.5 and ~3.8 nm can be apparently witnessed in the pore size distribution curve of CNTs/MC-Y (10/3/100) hybrid, further verifying its mesoporous feature.

Figure 4 displays the X-ray photoelectron spectroscopy (XPS) spectra of CNTs/MC-Y (10/3/100) hybrid. From the XPS survey spectrum in Fig. 4(a), C 1s, O 1s, N 1s

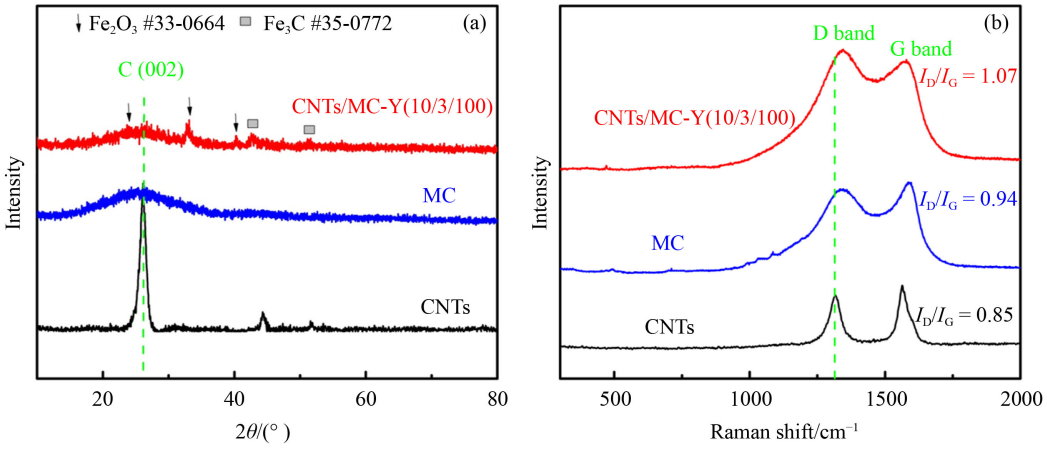

Fig. 3 (a) XRD patterns and (b) Raman spectra of CNTs, MC and CNTs/MC-Y (10/3/100) hybrid.

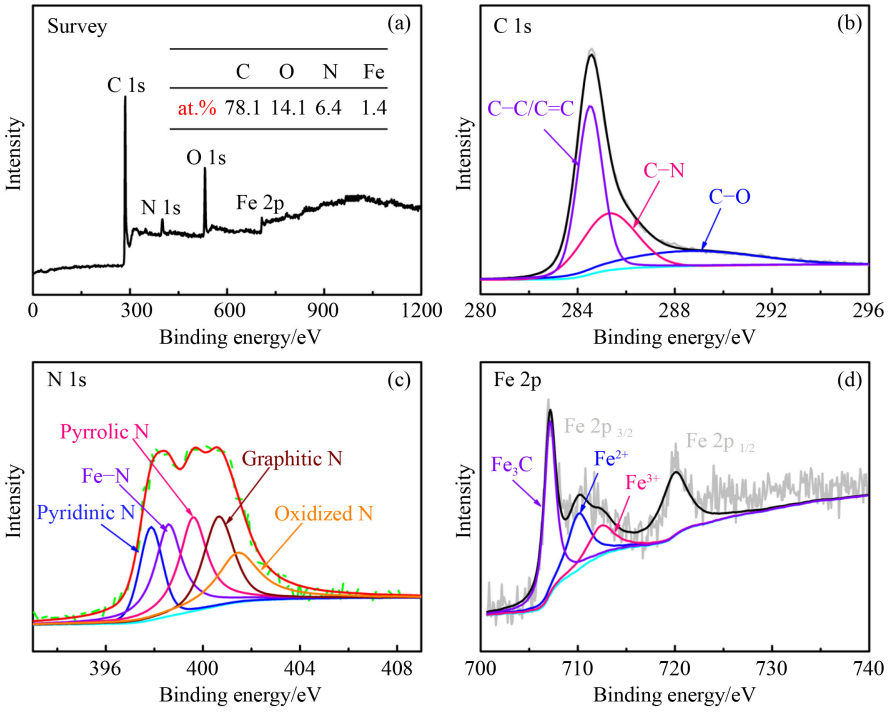

Fig. 4 (a) XPS survey spectrum, HR (b) C 1s, (c) N 1s and (d) Fe 2p spectra of CNTs/MC-Y (10/3/100) hybrid.

and Fe 2p peaks can be clearly evidenced, demonstrating successful N doping and possible formation of Fe_2O_3 and Fe_3C. As shown in Fig. 4(b), the HR C 1s peak can be deconvoluted into three different configurations: C–C/C=C (284.5 eV), C–N (285.3 eV) and C–O (288.5 eV) [37]. The presence of C–N bond also indicates effective N doping in carbon matrix. As for the HR N 1s peak in Fig. 4(c), it can be fitted into five various configurations: pyridinic N (397.8 eV), Fe–N (398.6 eV), pyrrolic N (399.6 eV), graphitic N (400.6 eV) and oxidized N (401.4 eV) [38–40]. Previous studies have confirmed that pyridinic N facilitates the adsorption of O_2 molecules and breaking of O–O bond [41,42]; pyrrolic N usually locates at the edge of carbon planes, and enhances lithium adsorption capability for Li^+ due to its defect property [43,44]; graphitic N with unpaired electron can accelerate the mobility of charge carrier and improve the conductivity [45]. While the existence of Fe–N structure can adjust the state density of carbon near the Fermi level, and lower the local work function, thus promoting the intrinsic activity towards ORR [46]. Figure 4(d) displays the HR Fe 2p spectra. The peak at 707.1 eV corresponds to the existence of Fe_3C. Previous literatures uncover that the presence of Fe_3C not only plays a role of an electrocatalyst to boost the conversion reversibility of solid electrolyte interface (SEI) film, but also changes the electronic state of carbon matrix, thus improving the surface reaction kinetics and providing more active sites for lithium storage [47]. Apart from the impact on LIBs, the effect of Fe_3C on the ORR performance has also been explored [48]. It is generally acknowledged that Fe_3C does not take part in ORR in a straightforward way, but it can provide extra electron for the exterior orbital of surrounding carbon atoms, which benefits the activation of O_2 during ORR. With regard to the peaks at 709.9 and 712.5 eV, they can be assigned to the Fe^{2+} and Fe^{3+} species, respectively. The existence of Fe^{2+} species is in favor of the formation of active Fe–N structure.

To explore the formation mechanism of CNTs/MC-Y (10/3/100) hybrid, the roles of three employed components (biomass precursors, transition metal inorganic salts and melamine) were systematically investigated. Firstly, to check the effect of biomass precursors, we substituted yeast with chitosan, glucose and sucrose to prepare CNTs/MC-C (10/3/100), CNTs/MC-G (10/3/100) and CNTs/MC-S (10/3/100). For better comparison, CNTs/MC-Y (0/3/100) was also produced by similar procedure without adding any biomass precursor. Figure S5 (cf. ESM) provides the SEM images of the corresponding products. Clearly, the introduction of any kind of biomass precursor can make successful growth of CNTs, while no biomass precursor only leads to the formation of large blocks. Undoubtedly, the initial biomass precursor acts as the main carbon source for the growth of CNTs. Analogous to conventional CVD strategy, the employed biomass precursor will be unstable under high temperature, and decompose into small and light-weight gaseous intermediates (such as hydrocarbons and alcohols), which can be further catalyzed by transition metals to produce CNTs.

To study the effect of transition metal inorganic salts, CNTs/MC-Y (10/0/100), CNTs/MC-Y (10/1.5/100) and CNTs/MC-Y (10/6/100) were synthesized with similar method by altering the dosages of initial metal salts. In the meanwhile, $CoCl_2{\cdot}6H_2O$ and $NiCl_2{\cdot}6H_2O$ with the same mass proportion as $FeCl_3{\cdot}6H_2O$ were used to prepare the corresponding products, which were denoted as CNTs/MC-Co (10/3/100) and CNTs/MC-Ni (10/3/100), respectively. The SEM images of these prepared samples were presented in Fig. S6 (cf. ESM). Figures S6(a–c) show the SEM images of CNTs/MC-Y with different adding amounts of $FeCl_3{\cdot}6H_2O$. Obviously, without adding metal salt, the CNTs/MC-Y (10/0/100) displays curly porous stacked carbon blocks. The formation of curly porous feature mostly ascribes to the attacking of NH_3 decomposed from melamine on the biomass-derived carbon [49]. With respect to CNTs/MC-Y (10/1.5/100), no CNTs can be captured, indicating that inadequate metal salt cannot effectively catalyze the growth of CNTs. While for CNTs/MC-Y (10/6/100), only a small quantity of CNTs can be found, and the majority of the product is big carbon chunk. This phenomenon may be due to the fact that superfluous metal-based particles seriously obstruct the pores of carbon blocks, thus restraining the growth of CNTs. In addition to these results, it can be seen from Figs. S6(d–e) that other metal salts (such as Co or Ni salts) also can catalyze the growth of CNTs during high-temperature pyrolysis process.

To probe the effect of melamine, CNTs/MC-Y (10/3/0), CNTs/MC-Y (10/3/10) and CNTs/MC-Y (10/3/500) were all synthesized by changing the dosages of melamine. The SEM images of these samples were displayed in Fig. S7 (cf. ESM). As exhibited in Figs. S7(a–b), CNTs fail to grow when the adding amount of melamine is not enough. This result is probably because no or insufficient melamine cannot release adequate NH_3 to promise the catalytic capability of metal catalyst. By contrast, the SEM image of CNTs/MC-Y (10/3/500) in Fig. S7(c) exhibits stripped flakes with relatively rough surface, which is mostly due to the fact that layered g-C_3N_4 nanosheets decomposed from excessive melamine act as a soft template to guide the growth of amorphous carbon.

Apart from the above-mentioned investigations, the effect of pyrolytic temperature was also probed. Herein, we annealed the mixed yeast/$FeCl_3{\cdot}6H_2O$/melamine composite at 600, 700 and 900 °C, respectively, and the corresponding products were labeled as CNTs/MC-600 (10/3/100), CNTs/MC-700 (10/3/100) and CNTs/MC-900 (10/3/100). It can be witnessed from the SEM images in Fig. S8 (cf. ESM) that too low temperature at 600 °C cannot efficiently catalyze the growth of CNTs, and relatively low temperature at 700 °C just leads to the formation of very short CNTs. While if the temperature

increases to 900 °C, only few CNTs can be observed. This result may attribute to the fact that too high temperature causes the structure collapse of carbon framework and dramatically reduces carbon porosity, which further hinders the growing channels and restrains the growth of CNTs.

Based on series of comparison and analysis, there is no doubt that biomass can be successfully converted to carbon nanomaterials by direct pyrolysis process. Moreover, the presence of three components (including biomass, transition metal inorganic salts and melamine) and precise control of their dosage become the key to the conversion of biomass to 3D CNTs/MC hybrids. And the possible conversion mechanism (see Fig. 5) can be depicted as follows. Firstly, some unstable part of biomass was pyrolyzed to release organic volatiles (such as hydrocarbons and alcohols), which act as the main carbon source for the growth of CNTs. Meanwhile, the residue of biomass condenses and crosslinks to establish MC. During high-temperature pyrolysis process, melamine can decompose into NH_3, which provides a reductive atmosphere and help the metal catalyst catalyze the growing of CNTs by a "tip-growth" mode. Specifically, the organic volatiles decomposed from biomass firstly deposit onto the surface of metal catalyst, and then diffuse downward to provide carbon source for the growth of CNTs. Subsequently, with the gradual growing of CNTs, the metal catalyst breaks away from the MC substrate due to the weak interaction between metal catalyst and MC substrate. Finally, the *in-situ* growth of CNTs will stop when the metal catalyst is completely encapsulated by excessive carbon layer. As a result, the 3D CNTs/MC hybrid can be produced.

3.2 Electrochemical performance

3.2.1 LIBs anode performance

The lithium storage performance of the CNTs/MC-Y (10/3/100) hybrid electrode was evaluated by cyclic voltammetry (CV), galvanostatic charge/discharge and electrochemical impedance spectroscopy (EIS) techniques (see Fig. 6). As betrayed from the CV curves in Fig. 6(a), in the first cathodic scan on CNTs/MC-Y (10/3/100) hybrid electrode, an inconspicuous peak below 0.2 V, a broad peak at ~0.5 V and a sharp peak at ~1.2 V can be observed, which correspond to the intercalation of Li^+, formation of SEI film and conversion of Fe^{3+} to Fe,

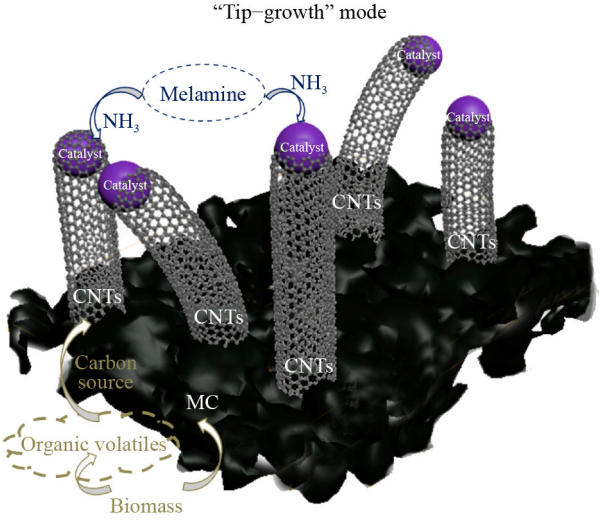

Fig. 5 The conversion mechanism of biomass to 3D CNTs/MC hybrid.

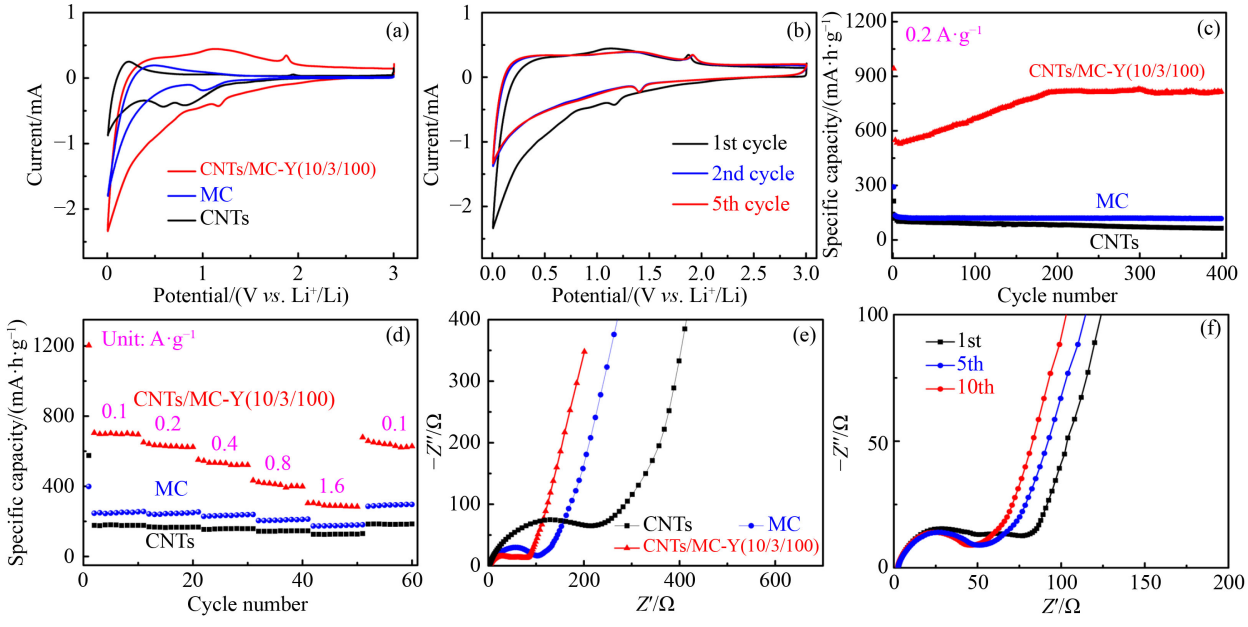

Fig. 6 (a) CV curves on different electrodes at 0.5 $mV \cdot s^{-1}$ for the first cycle; (b) CV curves on the CNTs/MC-Y (10/3/100) electrode at 0.5 $mV \cdot s^{-1}$ for the initial five cycles; (c) long-term cycling performance and (d) rate capability of different electrodes; (e) Nyquist plots on different electrodes for the first cycle; (f) Nyquist plots on the CNTs/MC-Y (10/3/100) electrode for various cycles.

respectively [50,51]. While in the first anodic scan, two weak peaks at ~0.3 and ~1.1 V and one peak at ~1.8 V can be assigned to the extraction of Li^+ from carbon interlayers and structure defects and transformation from Fe to Fe^{3+}. By comparison, the intensity of the reduction peak assigned to the formation of SEI film on CNTs/MC-Y (10/3/100) hybrid electrode is stronger than those on CNTs and MC electrodes, which is mostly related to the large SSA and catalyzation effect of tiny Fe_3C on electrolyte decomposition [47]. Figure 6(b) presents the initial five cycles on the CNTs/MC-Y (10/3/100) hybrid electrode. Clearly, after the first cycle, the subsequent CV curves almost overlap, indicating excellent cycling stability [52].

Figure 6(c) displays the cycling performance of the three samples at the current density of 0.2 $A \cdot g^{-1}$. It was discerned that the initial discharge capacities of CNTs and MC electrodes are 213 and 291 $mA \cdot h \cdot g^{-1}$, and these values kept as low as ~100 and ~120 $mA \cdot h \cdot g^{-1}$ respectively after 10 cycles. In contrast, the initial discharge capacity of CNTs/MC-Y (10/3/100) electrode reaches as high as 942 $mA \cdot h \cdot g^{-1}$. Though the discharge capacity rapidly decreases to 567 $mA \cdot h \cdot g^{-1}$ as the SEI film establishes on the electrode interface after the first cycle, this value gradually increases to over 800 $mA \cdot h \cdot g^{-1}$ after 180 cycles. This phenomenon is mostly due to the gradual electrolyte infiltration and electrode activation. Additionally, the decomposition and optimization of electrolyte-derived surface layer during cycling process also contribute to the growing of capacity [53]. After continuous 400 cycles, the discharge capacity still retains as high as 815 $mA \cdot h \cdot g^{-1}$, demonstrating excellent cycling capability. Meanwhile, the cycling performance of CNTs/MC-Y (10/3/100) electrode was also detected at a high current density of 0.5 $A \cdot g^{-1}$, as shown in Fig. S9 (cf. ESM). Clearly, even at higher current density, the electrode still presents a very high discharge capacity of 893 $mA \cdot g^{-1}$ even after long cycle life of 800 cycles, suggesting outstanding cycling performance.

Figure 6(d) shows the rate performance. The CNTs/MC-Y (10/3/100) electrode delivers a steady discharge capacity of ~700 $mA \cdot h \cdot g^{-1}$ at 0.1 $A \cdot g^{-1}$, and this value retains as ~290 $mA \cdot h \cdot g^{-1}$ even at a high current density of 1.6 $A \cdot g^{-1}$. When the current density reverts to 0.1 $A \cdot g^{-1}$, the discharge capacity recovers to ~630 $mA \cdot h \cdot g^{-1}$. By comparison, the CNTs and MC electrodes exhibit much smaller discharge capacities than the CNTs/MC-Y (10/3/100) electrode at all various current densities. Meanwhile, it was found that the discharge capacities of these two electrodes only get back to ~185 and ~293 $mA \cdot h \cdot g^{-1}$, respectively, when the current density returns to 0.1 $A \cdot g^{-1}$. Obviously, these results reflect that CNTs/MC-Y (10/3/100) electrode possesses much better rate capability than the counterparts.

To study the electrochemical kinetics behavior of CNTs/MC-Y (10/3/100) electrode, EIS technique was conducted. Figure 6(e) shows the Nyquist plots of three different electrodes before cycling, which consist of a depressed semicircle in the high-frequency region and an inclined line in the low-frequency region [54]. It is generally believed that the semicircle is related to the charge transfer resistance (R_{ct}), while the inclined line is concerned with the Warburg impedance during Li^+ diffusion process. Herein, all these plots are simulated by the equivalent circuit shown in Fig. S10 (cf. ESM). It was found that the fitted R_{ct} value (74.5 Ω) of CNTs/MC-Y (10/3/100) electrode is much smaller than those of CNTs (227.1 Ω) and MC (104.3 Ω) electrodes, respectively, indicating much faster kinetics toward charge transfer. In the meantime, the slope of the inclined line for CNTs/MC-Y (10/3/100) electrode is proven to be larger than those for CNTs and MC electrodes, showing smaller Li^+ diffusion resistance. Figure 6(f) exhibits the Nyquist plots of CNTs/MC-Y (10/3/100) electrode at different cycles. It was observed that the R_{ct} value gradually decays from the 1st cycle to the 10th cycle, suggesting an activation process and improved reversibility.

As reflected from the above analysis and discussion, the CNTs/MC-Y (10/3/100) electrode displays significantly improved lithium storage performance than the counterparts, which can be mostly ascribed to the following reasons. Firstly, 3D architecture and large SSA not only provide abundant accessible channels for ions transport and electrons transfer, but also afford much more active sites for lithium storage. Secondly, N doping not only further enhances the electrical conductivity of the hybrid electrode, but also offers extra sites for lithium storage. Apart from these, the existence of Fe_2O_3 can also contribute much stronger lithium storage capability on the basis of conversion reaction mechanism, and the embedded Fe_3C is demonstrated to play a role of catalyzing the formation of SEI film and speeding up the insertion of Li^+, hence enhancing the battery performance [47].

3.2.2 Electrocatalytic performance for ORR and ZABs batteries

3.2.2.1 ORR performance

The ORR performance of the samples was evaluated by CV and linear sweeping voltammogram (LSV) techniques (see Fig. 7). Figure S11 (cf. ESM) presents the CV curves on CNTs/MC-Y (10/3/100) electrode in N_2 and O_2 saturated 0.1 $mol \cdot L^{-1}$ KOH electrolyte. Clearly, the CV curve measured in N_2 saturated electrolyte shows a quasi-rectangular capacitive background, while an obvious reduction peak appears in the CV curve tested in O_2 saturated electrolyte, demonstrating the occurrence of ORR. Similar to the CNTs/MC-Y (10/3/100) electrode (see Fig. 7(a)), other comparison samples (CNTs and MC) also exhibit ORR reduction peaks in the CV curves recor-

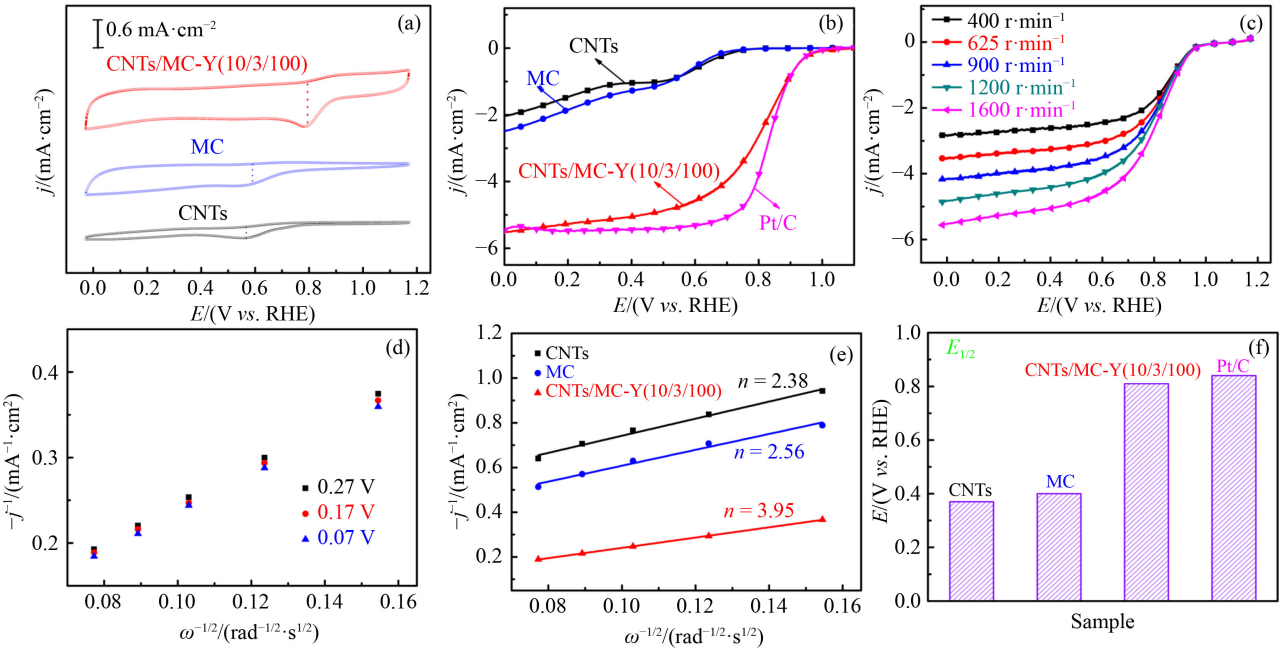

Fig. 7 (a) CV curves on different electrodes in oxygen saturated 0.1 mol·L^{-1} KOH electrolyte; (b) LSV curves on different electrodes at the rotation rate of 1600 r·min^{-1}; (c) LSV curves on CNTs/MC-Y (10/3/100) electrode at various rotation speeds in 0.1 mol·L^{-1} KOH electrolyte; (d) K–L plots on CNTs/MC-Y (10/3/100) electrode at various potentials in 0.1 mol·L^{-1} KOH electrolyte; (e) K–L plots on different electrodes at 0.17 V; (f) comparison of $E_{1/2}$ values on different electrodes.

ded in O_2 saturated electrolyte. Nevertheless, the peak potential for CNTs/MC-Y (10/3/100) electrode (0.80 V) is much more positive than those for CNTs (0.57 V) and MC (0.58 V) electrodes, indicating higher ORR activity. Figure 7(b) gives the LSV curves on different electrodes at 1600 r·min^{-1}. It was evidenced that the onset potential of CNTs/MC-Y (10/3/100) electrode shifts to 1.01 V, which appears more positive than those of the counterparts. Also, the limiting current density of CNTs/MC-Y (10/3/100) electrode (5.57 mA·cm^{-2}) is proven to be much larger than those of CNTs (2.10 mA·cm^{-2}) and MC (2.56 mA·cm^{-2}) electrodes. Impressively, the onset potential and limiting current density of CNTs/MCY (10/3/100) electrode is nearly approaching to those of commercial Pt/C electrode, demonstrating superior ORR performance.

To gain deep insight into the ORR kinetics of various electrodes, the LSV curves at different rotation speeds were presented in Figs. 7(c) and S12 (cf. ESM). In accordance with the Koutechy–Levich (K–L) equation, the corresponding K–L profiles were attained. Figure 7(d) gives the K–L plots on CNTs/MC-Y (10/3/100) electrode between 0.07 and 0.27 V. It is found that the electron transfer number (n) floats around 4.00, indicating almost four-electron ORR process. Figure 7(e) presents the K–L plots on different electrodes at 0.17 V. It was calculated that the n value of CNTs/MC-Y (10/3/100) electrode is 3.95, which is proven to be much larger than those on CNTs (2.38) and MC (2.56) electrodes, demonstrating much faster kinetics. Besides, we also compared the half-wave potential ($E_{1/2}$) values of different electrodes, as seen from Fig. 7(f). It was observed that the CNTs/MC-Y (10/3/100) electrode displays more positive $E_{1/2}$ value (0.81 V) than those (0.37 and 0.40 V) of other two counterparts, also reflecting much better ORR performance. For better comparison, the ORR performance of previously reported biomass-derived carbon catalysts was surveyed and summarized in Table S2 (cf. ESM). It can be evidenced that our prepared CNTs/MC-Y (10/3/100) exhibits comparable ORR performance with these reported biomass-derived carbon catalysts.

To meet the requirement of practical application, cycling durability and resistance to methanol poisoning were also tested, as shown in Fig. S13 (cf. ESM). Figure S13(a) provides the chronoamperometric testing result. Clearly, with respect to CNTs/MC-Y (10/3/100) electrode, the decay rate of current density is less than 3% even after long-period cycles, while this value increases to 18% for Pt/C electrode, verifying excellent cycling durability. Figure S13(b) shows the chronoamperometric response for CNTs/MC-Y (10/3/100) and Pt/C electrodes under the condition of adding 3 mol·L^{-1} methanol. Clearly, a quick decline of current density happens on Pt/C electrode at the moment of adding methanol, while no obvious recession of current density emerges on CNTs/MC-Y (10/3/100) electrode, indicating outstanding tolerance to methanol poisoning.

As analyzed above, the CNTs/MC-Y (10/3/100) electrode shows much better ORR performance than the counterparts, and this much enhanced ORR performance

is contributed by three aspects. Firstly, the unique 3D architecture and large SSA not only favor rapid electrolyte infiltration and ions/electrons transfer, but also benefit the exposure of catalytic sites, thus accelerating the ORR kinetics. Secondly, N doping plays an important role in improving the conductivity of carbon matrix and acts as catalytic sites for ORR. Lastly, the residual tiny Fe_3C and Fe_2O_3 in carbon matrix can also promote the ORR performance *via* weakening the O–O bond by Fe–O interaction, thus reducing the related reaction energy barrier.

3.2.2.2 ZABs batteries performance

To check the practical applicability of the catalyst, liquid ZABs were assembled by employing CNTs/MC-Y (10/3/100) as the cathode catalyst. A Zn foil and 6 mol·L^{-1} KOH aqueous solution containing 0.2 mol·L^{-1} zinc acetate were used as anode and electrolyte, respectively. For comparison, Pt/C catalyst was constructed into ZABs under identical conditions. The related electrochemical performance was displayed in Fig. 8. As seen from Fig. 8(a), the open-circuit potential of ZABs loaded with CNTs/MC-Y (10/3/100) catalyst keeps a steady value of 1.43 V, which proves slightly higher than that of the benchmark Pt/C catalyst (1.37 V after 400 s). Figure 8(b) presents the galvanostatic discharge tests at a current density of 5 mA·cm^{-2}. The specific capacity of ZABs with CNTs/MC-Y (10/3/100) catalyst is calculated to be 734 mA·h·g_{Zn}^{-1}, exceeding that (685 mA·h·g_{Zn}^{-1}) of ZABs with Pt/C catalyst. Furthermore, it was observed that the ZABs equipped with CNTs/MC-Y (10/3/100) catalyst show a steady discharge potential of 1.27 V with a decay of less than 0.03 V even after long-time working, indicating superior stability.

The rate performance of ZABs driven by CNTs/MC-Y (10/3/100) catalyst was measured at different current densities. As shown in Fig. 8(c), a steady voltage of 1.26 V can be discerned on the cathode with CNTs/MC-Y (10/3/100) catalyst even at a high current density of 10 mA·cm^{-2}, and this voltage nearly recovers to the initial value at the moment that the current density reduces to 1 mA·cm^{-2}, suggesting outstanding reversibility. Meanwhile, we found that the discharge potentials on the cathode with CNTs/MC-Y (10/3/100) catalyst are clearly higher than those on the cathode with Pt/C catalyst at any provided current densities, showing excellent rate performance. In addition, the peak power density is regarded as an important parameter in determining the energy conversion efficiency of the whole ZABs. As reflected from Fig. 8(d), the peak power density of ZABs constructed by CNTs/MC-Y (10/3/100) catalyst comes up to ~135.8 mW·cm^{-2} at 0.218 A·cm^{-2}, which surpasses that of Pt/C catalyst (114.7 mW·cm^{-2} at 0.191 A·cm^{-2}), exhibiting superior ORR activity.

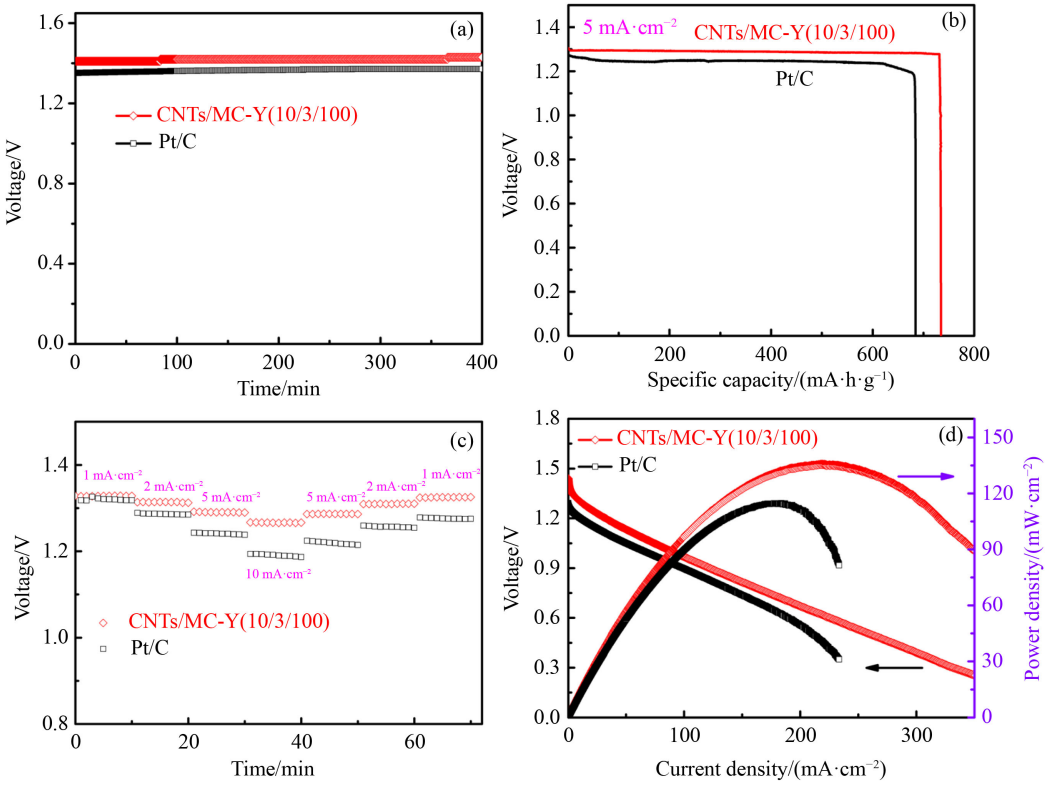

Fig. 8 (a) Open-circuit plots, (b) discharge curves at 5 mA·cm^{-2}, (c) discharge curves at various current densities and (d) discharge polarization and power density curves of Zn-air batteries driven by CNTs/MC-Y (10/3/100) and Pt/C catalysts.

4 Conclusions

In summary, a simple and scalable one-step pyrolysis strategy is proven to be practical to prepare 3D CNTs/MC architecture by using biomass, transition metal inorganic salts and melamine as initial precursors. It is demonstrated that each component in the initial precursors is indispensable, and suitable dosage of each component is proven to be the prerequisite for successful conversion of biomass to the final carbon nanomaterials. On account of the unique 3D architecture and joint virtues of CNTs and MC, the attained CNTs/MC hybrid presents versatile application toward LIBs and ZABs. When this 3D carbon hybrid is used as the anode for LIBs, it retains a very high discharge capacity of 893 $mA \cdot g^{-1}$ at a current density of 0.5 $A \cdot g^{-1}$ even after 800 cycles. Besides, this hybrid catalyst exhibits an ideal four electron pathway toward ORR. Additionally, the ZABs equipped with CNTs/MC-Y (10/3/100) catalyst displays a specific capacity as high as 734 $mA \cdot h \cdot g_{Zn}^{-1}$ at 5 $mA \cdot cm^{-2}$ and a peak power density reaching ~135.8 $mW \cdot cm^{-2}$ at 0.218 $A \cdot cm^{-2}$, which surprisingly exceed those of commercial Pt/C catalyst. Our results demonstrate the great application potential of 3D CNTs/MC architecture for energy storage and conversion systems.

Acknowledgements This work was financially supported by the National Key Research and Development Program of China (Grant No. 2019YFC1907900), Science & Technology Talents Lifting Project of Hunan Province (Grant No. 2022TJ-N16) and the Scientific Research Fund of Hunan Provincial Education Department, China (Grant No. 21A0392).

Electronic Supplementary Material Supplementary material is available in the online version of this article at https://dx.doi.org/10.1007/s11705-022-2266-8 and is accessible for authorized users.

References

1. Titirici M, White J, Brun N, Budarin L, Su S, del Monte F, MacLachlan J. Sustainable carbon materials. Chemical Society Reviews, 2015, 44(1): 250–290
2. Liu X, Dai L. Carbon-based metal-free catalysts. Nature Reviews Materials, 2016, 1(11): 16064
3. Yan J, Wang Q, Wei T, Fan Z. Recent advances in design and fabrication of electrochemical supercapacitors with high energy densities. Advanced Energy Materials, 2014, 4(4): 1300816
4. Zhang Q, Cheng X, Huang J, Peng H, Wei F. Review of carbon materials for advanced lithium−sulfur batteries. Carbon, 2015, 81: 850
5. Liu H, Liu X, Li W, Guo X, Wang Y, Wang G, Zhao D. Porous carbon composites for next generation rechargeable lithium batteries. Advanced Energy Materials, 2017, 7(24): 1700283
6. Zheng M, Chi Y, Hu Q, Tang H, Jiang X, Zhang L, Xu Q. Carbon nanotube-based materials for lithium−sulfur batteries. Journal of Materials Chemistry A: Materials for Energy and Sustainability, 2019, 7(29): 17204–17241
7. Dai L, Chang W, Baek B, Lu W. Carbon nanomaterials for advanced energy conversion and storage. Small, 2012, 8(8): 1130–1166
8. Kim M, Park T, Wang C, Tang J, Lim H, Hossain M, Konarova M, Yi J, Na J, Kim J, Yamauchi Y. Tailored nanoarchitecturing of microporous ZIF-8 to hierarchically porous double-shell carbons and their intrinsic electrochemical property. ACS Applied Materials & Interfaces, 2020, 12(30): 34065–34073
9. Kim M, Xu X, Xin R, Earnshaw J, Ashok A, Kim J, Park T, Nanjundan A K, El-Said W A, Yi J, Na J, Yamauchi Y. KOH-activated hollow ZIF-8 derived porous carbon: nanoarchitectured control for upgraded capacitive deionization and supercapacitor. ACS Applied Materials & Interfaces, 2021, 13(44): 52034–52043
10. Gupta N, Gupta M, Sharma K. Carbon nanotubes: synthesis, properties and engineering applications. Carbon Letters, 2019, 29(5): 419–447
11. Moothi K, Iyuke S, Meyyappan M, Falcon R. Coal as a carbon source for carbon nanotube synthesis. Carbon, 2012, 50(8): 2679–2690
12. Hoang V C, Hassan M, Gomes V G. Coal derived carbon nanomaterials recent advances in synthesis and applications. Applied Materials Today, 2018, 12: 342–358
13. Zhang G, Liu X, Wang L, Fu H. Recent advances of biomass derived carbon-based materials for efficient electrochemical energy devices. Journal of Materials Chemistry A: Materials for Energy and Sustainability, 2022, 10(17): 9277–9307
14. Zhang S, Jiang F, Huang B C, Shen X C, Chen W J, Zhou T P, Yu H Q. Sustainable production of value-added carbon nanomaterials from biomass pyrolysis. Nature Sustainability, 2020, 3(9): 753–760
15. Voloshin R A, Rodionova M V, Zharmukhamedov K, Nejat Veziroglu T, Allakhverdiev S I. Review: biofuel production from plant and algal biomass. International Journal of Hydrogen Energy, 2016, 41(39): 17257–17273
16. Osman A I, Mehta N, Elgarahy A M, Al Hinai A, Al Muhtaseb A H, Rooney D W. Conversion of biomass to biofuels and life cycle assessment: a review. Environmental Chemistry Letters, 2021, 19(6): 4075–4118
17. Alper K, Tekin K, Karagöz S, Ragauskas A J. Sustainable energy and fuels from biomass: a review focusing on hydrothermal biomass processing. Sustainable Energy & Fuels, 2020, 4(9): 4390–4414
18. Wang Z, Shen D, Wu C, Gu S. State-of-the-art on the production and application of carbon nanomaterials from biomass. Green Chemistry, 2018, 20(22): 5031–5057
19. Reina A, Jia X, Ho J, Nezich D, Son H, Bulovic V, Kong J. Large area, few-layer graphene films on arbitrary substrates by chemical vapor deposition. Nano Letters, 2009, 9(1): 30–35
20. Bi Z, Kong Q, Cao Y, Sun G, Su F, Wei X, Chen M. Biomass-derived porous carbon materials with different dimensions for supercapacitor electrodes: a review. Journal of Materials Chemistry A: Materials for Energy and Sustainability, 2019, 7(27): 16028–16045
21. Balahmar N, Mitchell A C, Mokaya R. Generalized mechanochemical synthesis of biomass-derived sustainable

carbons for high performance CO_2 storage. Advanced Energy Materials, 2015, 5(22): 1500867

22. Wang Y, Zhang M, Shen X, Wang H, Wang H, Xia K, Yin Z, Zhang Y. Biomass-derived carbon materials: controllable preparation and versatile applications. Small, 2021, 17(40): 2008079
23. Yin J, Zhang W, Alhebshi N, Salah N, Alshareef H. Synthesis strategies of porous carbon for supercapacitor applications. Small Methods, 2020, 4(3): 1900853
24. Lyu L, Seong K, Ko D, Choi J, Lee C, Hwang T, Cho Y, Jin X, Zhang W, Pang H, Piao Y. Recent development of biomass-derived carbons and composites as electrode materials for supercapacitors. Materials Chemistry Frontiers, 2019, 3(1): 2543–2570
25. Zhang M, Zhang J, Ran S, Sun W, Zhu Z. Biomass-derived sustainable carbon materials in energy conversion and storage applications: status and opportunities. A mini review. Electrochemistry Communications, 2022, 138: 107283
26. Yang W, Liu X, Yue X, Jia J, Guo S. Bamboo-like carbon nanotube/Fe_3C nanoparticle hybrids and their highly efficient catalysis for oxygen reduction. Journal of the American Chemical Society, 2015, 137(4): 1436–1439
27. Kang J, Duan X, Wang C, Sun H, Tan X, Tade M O, Wang S. Nitrogen-doped bamboo-like carbon nanotubes with Ni encapsulation for persulfate activation to remove emerging contaminants with excellent catalytic stability. Chemical Engineering Journal, 2018, 332: 398–408
28. Chen S, Bao P, Wang G. Synthesis of Fe_2O_3-CNT-graphene hybrid materials with an open three-dimensional nanostructure for high capacity lithium storage. Nano Energy, 2013, 2(3): 425–434
29. Yan N, Zhou X, Li Y, Wang F, Zhong H, Wang H, Chen Q. Fe_2O_3 nanoparticles wrapped in multi-walled carbon nanotubes with enhanced lithium storage capability. . Scientific Reports, 2013, 3(1): 3392
30. Zhang B, Li T, Huang L, Ren Y, Sun D, Pang H, Tang Y. *In situ* immobilization of Fe/Fe_3C/Fe_2O_3 hollow hetero-nanoparticles onto nitrogen-doped carbon nanotubes towards high-efficiency electrocatalytic oxygen reduction. Nanoscale, 2021, 13(10): 5400–5409
31. Bistamam M S A, Azam M A. Tip-growth of aligned carbon nanotubes on cobalt catalyst supported by alumina using alcohol catalytic chemical vapor deposition. Results in Physics, 2014, 4: 105–106
32. Gohier A, Ewels C P, Minea T M, Djouadi M A. Carbon nanotube growth mechanism switches from tip- to base-growth with decreasing catalyst particle size. Carbon, 2008, 46(10): 1331–1338
33. Behan J A, Mates Torres E, Stamatin S N, Domínguez C, Iannaci A, Fleischer K, Colavita P E. Oxygen reduction reaction: untangling cooperative effects of pyridinic and graphitic nitrogen sites at metal-free N-doped carbon electrocatalysts for the oxygen reduction reaction. Small, 2019, 15(48): 1970256
34. Li J, Zhang Y, Zhang X, Han J, Wang Y, Gu L, Song B. Direct transformation from graphitic C_3N_4 to nitrogen-doped graphene: an efficient metal-free electrocatalyst for oxygen reduction reaction. ACS Applied Materials & Interfaces, 2015, 7(35): 19626–19634
35. Yang L, Huang N, Lu C, Yu H, Sun P, Lv X, Sun X. Atomically dispersed and nanoscaled Co species embedded in micro-/mesoporous carbon nanosheet/nanotube architecture with enhanced oxygen reduction and evolution bifunction for Zn-air batteries. Chemical Engineering Journal, 2021, 404: 127112
36. Biemolt J, Rothenberg G, Yan N. Understanding the roles of amorphous domains and oxygen-containing groups of nitrogen-doped carbon in oxygen reduction catalysis: toward superior activity. Inorganic Chemistry Frontiers, 2020, 7(1): 177–185
37. Cheng J, Wu D, Wang T. N-doped carbon nanosheet supported Fe_2O_3/Fe_3C nanoparticles as efficient electrode materials for oxygen reduction reaction and supercapacitor application. Inorganic Chemistry Communications, 2020, 117: 107952
38. Tian Y, Xu L, Qian J, Bao J, Yan C, Li H, Zhang S. Fe_3C/Fe_2O_3 heterostructure embedded in N-doped graphene as a bifunctional catalyst for quasi-solid-state zinc-air batteries. Carbon, 2019, 146: 763–771
39. Zhang J, Zhang M, Zeng Y, Chen J, Qiu L, Zhou H, Zhu Z. Single Fe atom on hierarchically porous S, N-co doped nanocarbon derived from porphyra enable boosted oxygen catalysis for rechargeable Zn-air batteries. Small, 2019, 15(24): 1900307
40. Han J, Bao H, Wang J Q, Zheng L, Sun S, Wang Z L, Sun C. 3D N-doped ordered mesoporous carbon supported single-atom Fe-N-C catalysts with superior performance for oxygen reduction reaction and zinc-air battery. Applied Catalysis B: Environmental, 2021, 280: 119411
41. Wang X R, Liu J Y, Liu Z W, Wang W C, Luo J, Han X P, Yang J. Identifying the key role of pyridinic-N-co bonding in synergistic electrocatalysis for reversible ORR/OER. Advanced Materials, 2018, 30(23): 1800005
42. Takeyasu K, Furukawa M, Shimoyama Y, Singh S K, Nakamura J. Role of pyridinic nitrogen in the mechanism of the oxygen reduction reaction on carbon electrocatalysts. Angewandte Chemie International Edition, 2021, 60(10): 5121–5124
43. Gu S, Christensen T, Hsieh C T, Mallick B C, Gandomi Y A, Li J, Chang J K. Improved lithium storage capacity and high rate capability of nitrogen-doped graphite-like electrode materials prepared from thermal pyrolysis of graphene quantum dots. Electrochimica Acta, 2020, 354: 136642
44. He B, Li G, Chen L, Chen Z, Jing M, Zhou M, Hou Z. A facile N doping strategy to prepare mass-produced pyrrolic N-enriched carbon fibers with enhanced lithium storage properties. Electrochimica Acta, 2018, 278: 106–113
45. Li X F, Lian K Y, Liu L, Wu Y, Qiu Q, Jiang J, Luo Y. Unraveling the formation mechanism of graphitic nitrogen-doping in thermally treated graphene with ammonia. Scientific Reports, 2016, 6(1): 23495
46. Lai Q, Zheng L, Liang Y, He J, Zhao J, Chen J. Metal−organic-framework-derived Fe-N/C electrocatalyst with five-coordinated Fe-N_x sites for advanced oxygen reduction in acid media. ACS Catalysis, 2017, 7(3): 1655–1663
47. Chen L, Li Z, Li G, Zhou M, He B, Ouyang J, Hou Z. A facile self-catalyzed CVD method to synthesize Fe_3C/N-doped carbon nanofibers as lithium storage anode with improved rate capability

and cyclability. Journal of Materials Science and Technology, 2020, 44: 229–236

48. Xu C, Chen L, Wen Y, Qin S, Li H, Hou Z, Kuang Y. A co-operative protection strategy to synthesize highly active and durable Fe/N co-doped carbon towards oxygen reduction reaction in Zn-air batteries. Materials Today Energy, 2021, 21: 100721
49. Xu J, Wu C, Yu Q, Zhao Y, Li X, Guan L. Ammonia defective etching and nitrogen-doping of porous carbon toward high exposure of heme-derived Fe-N_x site for efficient oxygen reduction. ACS Sustainable Chemistry & Engineering, 2018, 6(1): 551–560
50. Liu Y, Li X, Haridas A K, Sun Y, Heo J, Ahn J H, Lee Y. Biomass-derived graphitic carbon encapsulated Fe/Fe_3C composite as an anode material for high-performance lithium ion batteries. Energies, 2020, 13(4): 827
51. Zheng J, Kong F, Tao S, Qian B A. Fe_2O_3-Fe_3C heterostructure encapsulated into a carbon matrix for the anode of lithium-ion batteries. Chemical Communications, 2021, 57(70): 8818–8821
52. Kim M, Fernando J F, Wang J, Nanjundan A K, Na J, Hossain M S A, Nara H, Martin D, Sugahara Y, Golberg D, Yamauchi Y. Efficient lithium-ion storage using a heterostructured porous carbon framework and its *in situ* transmission electron microscopy study. Chemical Communications, 2022, 58(6): 863–866
53. Chen X, Cheng X, Liu Z. High sulfur-doped hard carbon anode from polystyrene with enhanced capacity and stability for potassium-ion storage. Journal of Energy Chemistry, 2022, 68: 688–698
54. Kim M, Fernando J F, Li Z, Alowasheeir A, Ashok A, Xin R, Martin D, Nanjundan A K, Golberg D, Yamauchi Y, Amiralian N, Li J. Ultra-stable sodium ion storage of biomass porous carbon derived from sugarcane. Chemical Engineering Journal, 2022, 445: 136344